Mechanism of Delayed Storm Surges in Straits: Seiche-Induced Oscillations Triggered by Typhoon Passage

Shinichiro Ozaki[1], Yoshihiko Ide[2], and Masaru Yamashiro[2]

[1]Department of Civil Engineering, Graduate School of Engineering, Kyushu University, Fukuoka, Japan
[2]Disaster Risk Reduction Research Center, Faculty of Engineering, Kyushu University, Fukuoka, Japan

Correspondence: Shinichiro Ozaki (ozaki.shinichiro.247@s.kyushu-u.ac.jp)

Abstract. Storm surges are typically driven by a combination of low atmospheric pressure and strong winds associated with typhoons, with the maximum surge often occurring near the time of the typhoon's closest approach. However, during Typhoon Maysak (2020), delayed flooding was observed along the northern coast of Kyushu Island (NCKI), approximately 10 hours after the typhoon had passed. By that time, both atmospheric pressure and wind intensity had substantially weakened, indicating that conventional mechanisms—such as wind setup and the inverted barometer effect—could not fully account for the phenomenon. This study explores the mechanisms behind delayed storm surges along the NCKI through a combination of observational data analysis, storm surge simulations, and continuous wavelet transform (CWT) analysis. The results reveal that typhoons passing through the western channel of the Tsushima Strait (WCTS-type) frequently generate double-peaked storm surge anomaly, with the second peak being both larger and longer-lasting than the first. Spectral analysis identified dominant oscillations with periods of approximately 5 and 10 hours, corresponding to the natural modes of the Tsushima Strait. These oscillations, interpreted as (1,1) and (1,0) mode seiches, are excited by the release of potential energy trapped within the strait once the external forcing has subsided. Notably, the 5-hour mode appears to be strongly influenced by the Coriolis effect. Our findings reveal a previously unrecognized storm surge mechanism in which significant surges occur not during, but after, a typhoon's passage through a strait. This delayed response arises from resonant amplification caused by modal oscillations within the strait, particularly in cases where typhoon tracks curve westward. The study underscores the critical roles of strait geometry, natural oscillation modes, and the timing of external forcing in shaping storm surge behavior. These insights extend beyond the NCKI and are relevant to other semi-enclosed strait regions worldwide that exhibit similar meteorological and geographical characteristics, even though the extent of influence from oscillation modes, periods, and amplitudes may vary depending on the strait's horizontal scale, water depth, and latitude.

1 Introduction

Storm surges are events in which sea levels rise significantly due to low atmospheric pressure and strong winds, typically associated with typhoons. When a storm surge occurs, it can rapidly inundate low-lying coastal areas, causing widespread flooding. Climate projections that incorporate the effects of global warming indicate that storm surge heights are likely to increase globally (Balaguru et al. (2016); Yang et al. (2020); Mori et al. (2022)). To reduce the damage caused by storm surges, it is vital to implement both structural measures, such as storm surge barriers (Miguel Esteban (2014)), and non-structural measures, such as real-time forecasting systems (Igarashi and and (2021)). A comprehensive understanding of storm surge dynamics is therefore crucial for developing effective protection strategies.

Several widely accepted mechanisms explain the generation of storm surges. The inverted barometer effect accounts for sea-level rise caused by low atmospheric pressure (e.g., Wunsch and Stammer (1997)), while wind setup refers to the rise in sea level due to strong winds forcing seawater shoreward (e.g., Walton and Dean (2009)). This occurs when coastal winds drive surface water toward the shore, causing accumulation in shallow regions and elevating the local sea level. Wave setup, in contrast, results from wave breaking and radiation stress (e.g., Wu et al. (2018)). These mechanisms are typically most pronounced when a typhoon is closest to the target area, as wind speeds and pressure gradients peak during this time. Additional causes of storm surges include Ekman setup, wherein sustained winds blowing parallel to the coast induce shoreward water transport via the Coriolis effect (e.g., Kim et al. (2010), Shen and Gong (2009)), and the propagation of shelf waves, which carry elevated water levels along the coast after the storm (e.g., Kennedy et al. (2011)). Among these mechanisms, wind setup is generally recognized as the primary contributor to storm surge height. The magnitude of wind setup is directly proportional to the wind fetch and inversely proportional to water depth. Regions most vulnerable to major storm surges often include ocean-facing bays with geographical features that amplify wind-driven water accumulation (Bilskie et al. (2016); Bhaskaran et al. (2020); Nakajo et al. (2015); Ide et al. (2020)). Significantly, even in straits with relatively short fetch lengths, substantial storm surges can still occur due to wind setup. For instance, in East Asia, the Tsushima Strait is a significant waterway located within the Northwest Pacific region (Figure 1a). This strait is frequently impacted by typhoons. These typhoons often track northeast through the strait before either making landfall along the southern coast of the Korean Peninsula (SCKP) (Figure 1b) or continuing into the Sea of Japan. Typhoon Sanba—the strongest typhoon of 2012—passed through the Tsushima Strait, bringing maximum instantaneous wind speeds exceeding 20 m/s and storm surge heights over 100 cm at Gwangyang (Figure 1b), near the center of the SCKP region (Yoon et al. (2014)). Typically, when a typhoon traverses the western channel of the Tsushima Strait (WCTS), a significant storm surge is observed along the SCKP, primarily driven by wind setup. As illustrated in Figure 2a, when the typhoon is centered over the strait, the counterclockwise wind circulation characteristic of Northern Hemisphere typhoons generates strong onshore winds directed toward the SCKP. This results in substantial wind-driven water accumulation. Additionally, the surge is further enhanced by the inverted barometer effect, which raises sea level under conditions of low atmospheric pressure.

On the northern coast of Kyushu Island (NCKI) (Figure 1b), which lies across the Tsushima Strait from the SCKP, significant storm surges are generally considered unlikely during typhoon approaches. When a typhoon is located over the Tsushima

Strait, southwesterly winds typically prevail over the NCKI (Figure 2a). Because the winds drive seawater away from the coast, the local sea level tends to drop—opposite to the rise observed along the SCKP. However, during Typhoon Maysak (2020), widespread inundation occurred along the NCKI, causing flooding and major traffic disruptions (Niimi et al. (2022)). Although Typhoon Maysak passed through the WCTS, it did not make landfall on the NCKI (see Figure 3). Notably, flooding occurred approximately 10 hours after the typhoon's closest approach—by which time the typhoon had already moved more than 600 km away. Typically, once a typhoon enters the Sea of Japan after passing through the Tsushima Strait, its influence on the NCKI diminishes: strong winds subside (Figure 2b), and atmospheric pressure returns to near-normal sea level conditions. Therefore, the storm surge observed in this event cannot be attributed to the typical storm surge mechanisms such as wind setup, wave setup, or the inverted barometer effect, as the local pressure had risen to around 1,000 hPa and no strong winds were present at the time of inundation. Previous studies have suggested that delayed storm surges along the NCKI may be linked to oscillatory responses within the Tsushima Strait (e.g., Hong and Yoon (1992); Niimi et al. (2022)). While storm surge dynamics have been studied in other straits, such as the Taiwan Strait Zhang et al. (2010), the Strait of Georgia Soontiens et al. (2016), and the Singapore Strait Tkalich et al. (2013), these investigations do not report delayed surge responses following typhoon passage. In contrast, the Tsushima Strait appears to exhibit a unique behavior: storm surges can occur several hours after a typhoon has passed, likely due to natural oscillations within the strait.

Although storm surges along the NCKI have been documented in previous studies, the delayed occurrence of these surges following typhoon passage through the WCTS remains insufficiently understood. This study offers new insights into the phenomenon by highlighting the role of coastal topography in generating delayed surge responses. To investigate this, we analyzed multiple typhoon events from the past two decades, aiming to elucidate the mechanisms underlying post-passage surge increases, using the Tsushima Strait as a representative case study. Our analysis integrates observational records, numerical storm surge simulations, and spectral analysis via wavelet transforms. Through this approach, we identified dominant oscillation modes with periods of approximately 10 and 5 hours that were consistently present during delayed storm surge events.

The structure of this paper is organized as follows. Section 2 describes the geographical and oceanographic characteristics of the Tsushima Strait. Section 3 introduces the selected typhoons analyzed in this study. Section 4 presents the analysis of observed storm surges and meteorological data. Section 5 outlines the numerical simulations conducted to reproduce the storm surge behavior. Section 6 explains the application of continuous wavelet transform (CWT) for spectral analysis of the simulated results. Section 7 discusses the physical mechanisms behind the observed phenomena. Finally, Section 8 summarizes the main findings and implications of this study.
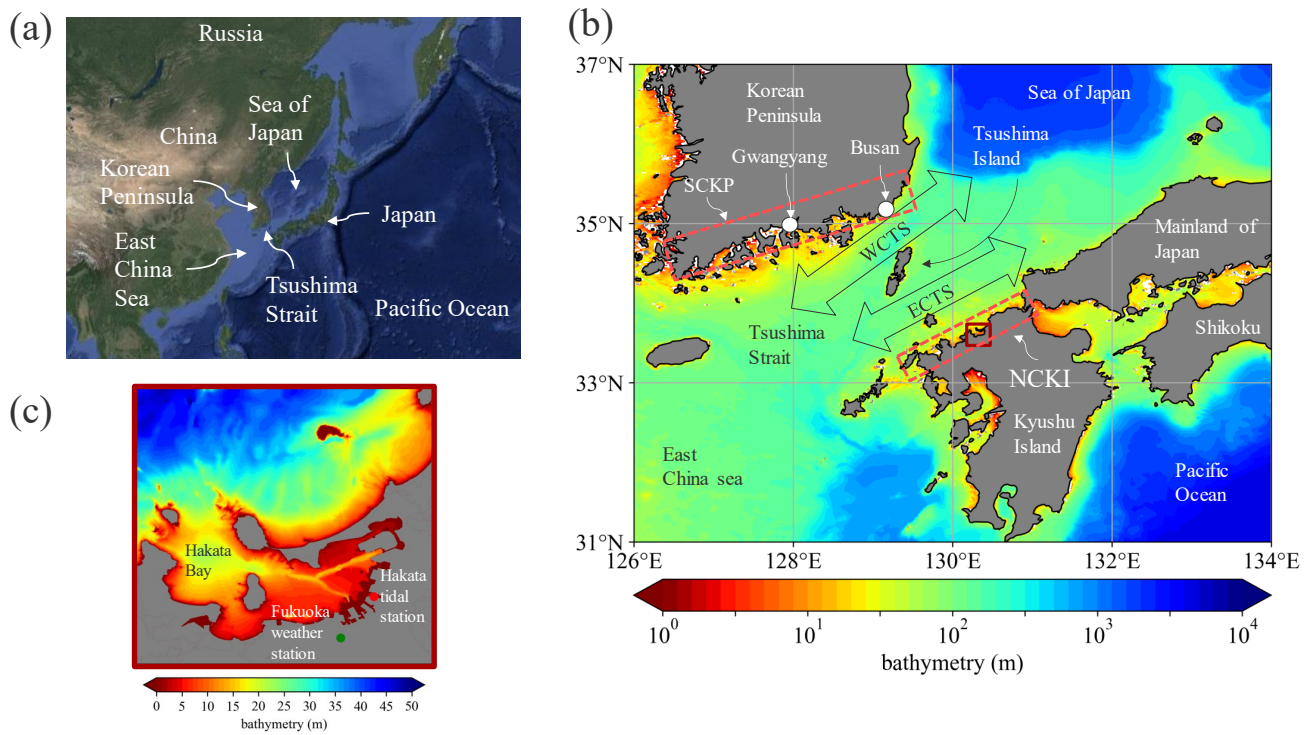
Figure 1. Bathymetric maps illustrating the geographical context and study regions. (a) Regional map displaying the Northwest Pacific. (b) Magnified view showing the detailed bathymetry of the Tsushima Strait. (c) Close-up view presenting the bathymetry within Hakata Bay.
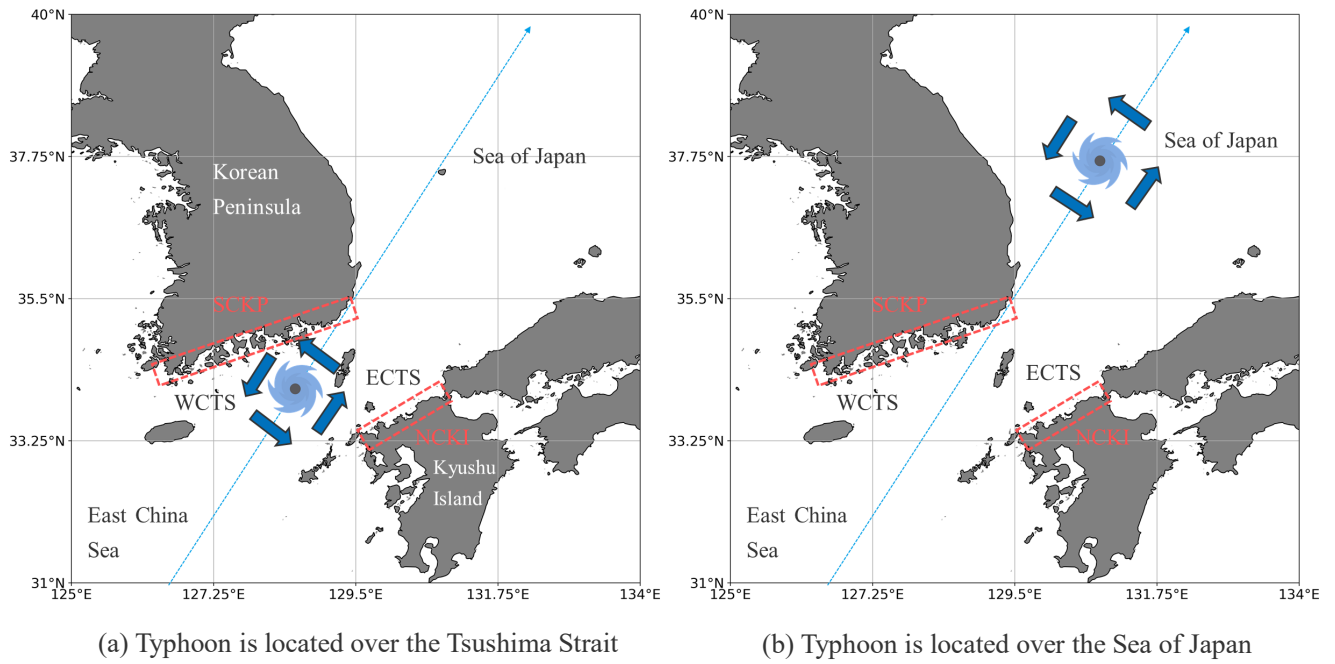
(a) Typhoon is located over the Tsushima Strait

(b) Typhoon is located over the Sea of Japan

typhoon   Wind direction

Figure 2. Schematic figure of typhoon positions and wind directions during its passage through the WCTS: (a) when the typhoon is located over the Tsushima Strait; (b) when the typhoon is located over the Sea of Japan.

2 Study Area

The Tsushima Strait, located in the Northwest Pacific region as shown in Figure 1a, is situated in East Asia between the Korean Peninsula to the northwest and Kyushu Island in Japan to the southeast (Figure 1b). This strait is a typical typhoon-prone region, particularly during the summer months, and frequently experiences strong winds and storm surges associated with typhoon passages. The average water depth of the strait is approximately 80 m. The strait connects two major bodies of water: the Sea of Japan to the north and the East China Sea to the south. The Sea of Japan is characterized by deep waters, while the East China Sea is comparatively shallow. This stark depth contrast contributes to the complex oceanographic dynamics within the strait. Tsushima Island is located in the center of the strait (Figure 1b), dividing it into two distinct channels: the WCTS, located between Tsushima Island and the SCKP, and the ECTS, located between Tsushima Island and the NCKI. Of the two, the WCTS is slightly deeper and plays a more significant role in water exchange and current dynamics across the strait.

Hakata Bay, located in the central part of the NCKI, is shown in the Figure 1c. The surrounding area includes Fukuoka City, one of the most densely populated urban centers in the region. The bay extends approximately 20 km east–west and 10 km north–south, forming a semi-enclosed coastal basin. The Hakata tidal station, situated on the eastern side of the bay, has provided continuous sea-level records since 1998. Additionally, the Fukuoka weather station, located on the southern side of the bay, continuously monitors atmospheric pressure, wind speed, and wind direction.

3 Selected Typhoons

We selected various typhoons for analysis through the following process. The tracks of the selected typhoons are shown in Figure 3. First, we obtained best track data for 1,898 typhoons recorded from 1951 to 2022 by the Japan Meteorological Agency (JMA; https://www.jma.go.jp/jma/jma-eng/jma-center/rsmc-hp-pub-eg/besttrack.html). The full set of typhoon tracks is shown in Figure 3a. Next, we identified 599 typhoons that occurred between 1998 and 2022, during which tide-level data were available at the Hakata tidal station (Figure 3b). From this subset, we then selected 67 typhoons whose tracks passed within a 300 km radius of the Hakata tidal station for detailed analysis (Figure 3c). To calculate storm surge anomalies associated with the 67 selected typhoons, we used the following method. First, sea-surface elevation data sampled at 30-second intervals from 1998 to 2022 were obtained from the Hakata tidal station via the Regional Delayed Mode Data Base (RDMDB, https://near-goos1.jodc.go.jp/vpage/search.html). Second, we performed harmonic analysis on the observed data using the pytides 0.0.4 package (https://github.com/sam-cox/pytides) to extract tidal constituents, including Z0, M2, S2, K1, O1, and others—a total of 39 components. Third, storm surge anomalies were calculated by subtracting the reconstructed astronomical tide from the observed sea-surface elevation. To remove interannual variability, we computed the average anomaly at the time of typhoon approach for each year and subtracted this mean value. Finally, we identified 16 typhoons that produced maximum storm surge anomalies of 30 cm or greater at the Hakata tidal station (Figure 3d).

The selected typhoons can be categorized into two types based on their tracks around the Tsushima Strait: WCTS-type and ECTS-type typhoons. WCTS-type typhoons follow a path from the SCKP through the WCTS, approaching the Hakata area from the northwest. This category includes Typhoons Rusa (2002), Maemi (2003), Megi (2004), Sanba (2012), Chaba (2016),

Kong-rey (2018), Maysak (2020), Haishen (2020), and Hinnamnor (2022). ECTS-type typhoons, on the other hand, move from the ECTS toward the NCKI, generally approaching from the northeast. This group includes Typhoons Bart (1999), Chaba (2004), Songda (2004), Shanshan (2006), Danas (2013), Goni (2015), and Tapah (2019). These two classifications are used throughout the following analysis.
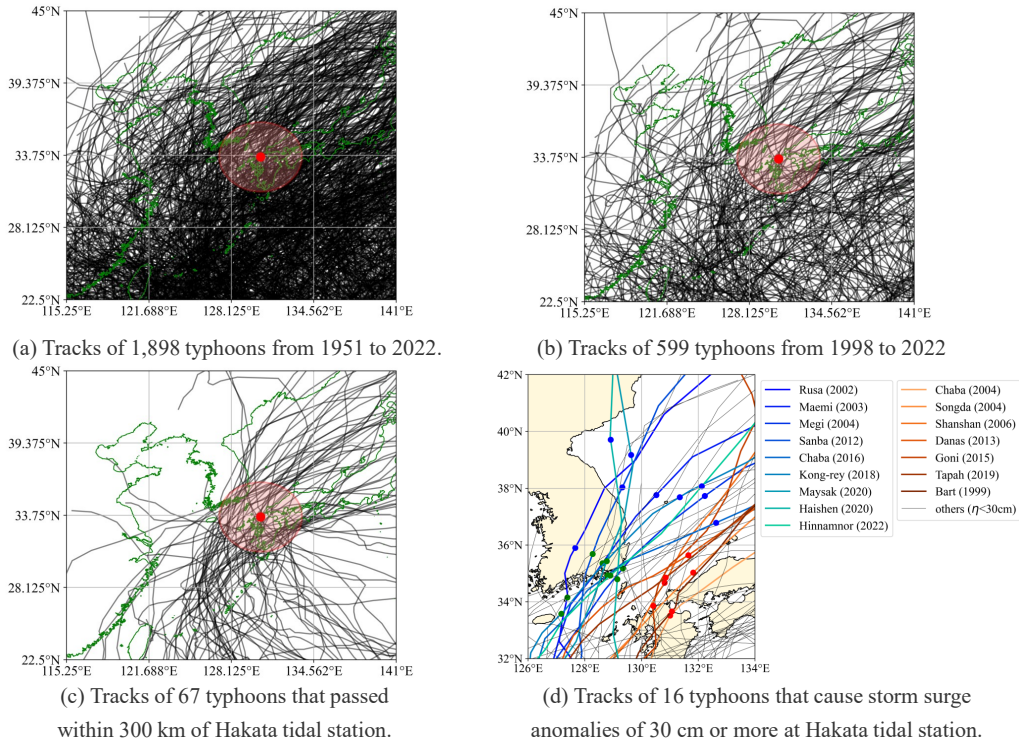

(a) Tracks of 1,898 typhoons from 1951 to 2022.

(b) Tracks of 599 typhoons from 1998 to 2022

(c) Tracks of 67 typhoons that passed within 300 km of Hakata tidal station.

(d) Tracks of 16 typhoons that cause storm surge anomalies of 30 cm or more at Hakata tidal station.

Figure 3. Tracks of selected typhoons in this study. (a) Tracks of 1,898 typhoons recorded by JMA from 1951 to 2022. (b) Tracks of 599 typhoons that occurred between 1998 and 2022, during which tide-level observations were available at the Hakata tidal station. (c) Tracks of 67 typhoons that passed within a 300 km radius of the Hakata tidal station. (d) Tracks of 16 typhoons that caused storm surge anomalies of 30 cm or more at the Hakata tidal station between 1999 and 2022. In panels (a)–(c), black curves represent typhoon tracks, the red dot indicates the location of the Hakata tidal station, and the red circle marks the 300 km radius around the station. In panel (d), red and blue lines show the tracks of the 16 typhoons that generated significant storm surge anomalies. Red lines correspond to ECTS-type typhoons, while blue lines correspond to WCTS-type typhoons. The remaining typhoons are shown in black lines. For WCTS-type typhoons, green dots indicate the timing of the first surge peak at the Hakata tidal station, and blue dots indicate the second peak. For ECTS-type typhoons, red dots indicate the timing of the maximum storm surge anomaly (as referenced by arrows in Figure 4).

4 Observed Storm Surge and weather data Characteristics

We examined the observed data, such as storm surge anomalies, wind, and atmospheric pressure, and categorized them according to the typhoon tracks. The black lines in Figure 4 shows the time series of storm surge anomalies acquired at the Hakata tidal station for both WCTS and ECTS-type typhoons.

storm surge anomalies during ECTS-type typhoons tend to rise sharply over a short period (indicated by purple arrows in Figure 4a). Typhoons Chaba (2004) and Bart (1999) exhibit a single peak in the storm surge anomaly, while Songda (2004), Shanshan (2006), Goni (2015), and Tapah (2019) display a second peak occurring within approximately two hours before or after the initial maximum. These double peaks are the result of a two-hour oscillation of the bay water in Hakata Bay, as previously reported by Yamashiro et al. (2016). Similar oscillatory responses may have occurred during Chaba (2004) and Bart (1999), although these were not clearly observed in tide-gauge records—possibly due to differences in typhoon translation speed or the timing of pressure variations. Among these cases, Typhoon Danas (2013) generated a relatively small maximum tidal anomaly and showed a more gradual temporal variation. Although Danas tracked directly over Tsushima Island, the presence of only one prominent peak in its time series of storm surge anomaly led to its classification as an ECTS-type event in this study. Similarly, Typhoon Holly (1984), which passed through the central Tsushima Strait, produced a modest peak and gentle fluctuation at the Hakata tidal station (Hong and Yoon (1992)). A detailed investigation into the surge-generation mechanisms of these two typhoons is left for future work.

The positions of the ECTS-type typhoons at the times indicated by the purple arrows in Figure 4a are marked with red dots along their tracks in Figure 3d. The peak storm surge anomaly is observed just after the typhoon passes over Hakata Bay. As a representative ECTS typhoon, Figure 5a shows the time series of the wind and air pressure at the Fukuoka weather station (see Figure 1c) during Goni (2015). At 08:00 on August 25, 2015, when the storm surge anomaly reaches its maximum, the air pressure also drops to its minimum value of 970 hPa, and a northerly wind is observed (purple arrows in Figure 5a). These observations indicate that the rapid rise in storm surge anomalies during ECTS-type typhoons can be attributed to a combination of the inverted barometer effect and wind setup. As these typhoons pass close to Hakata Bay, the sharp drop in atmospheric pressure causes a corresponding rise in sea level via the inverted barometer effect. Additionally, once the typhoon moves slightly beyond the bay, northerly onshore winds develop, inducing wind setup that further elevates the sea level.

In contrast, storm surge anomalies associated with WCTS-type typhoons exhibit unusual temporal patterns. Typically, the surge anomaly increases as the typhoon approaches Hakata Bay, reaching an initial peak (green dot in Figure 3; red arrow in Figures 4b). This is followed by a rapid decrease (blue arrow in Figures 4b), and then a second increase resulting in another peak (purple arrow in Figures 4b). The location of the typhoon at the time of the second peak is indicated by a blue dot in Figure 3, showing that the typhoon had already entered the Sea of Japan. Typhoon Sanba (2012) is a notable exception, as it did not exhibit this two-peaked pattern at the Hakata tidal station. Figure 5b presents the time series of wind and atmospheric pressure at the Fukuoka weather station during Typhoon Hinnamnor (2022). The first storm surge anomaly peak coincides with the typhoon's closest approach to the NCKI, when the minimum pressure of 991.4 hPa is recorded—consistent with the inverted barometer effect (red arrows in Figures 4b and 5b). However, the second peak occurs after the typhoon has moved into

155 the Sea of Japan, at which time local pressure at the NCKI rises to around 1,000 hPa, and wind speeds drop below 5 m/s (purple arrows in Figures 4b and 5b). Thus, this second surge peak cannot be explained by the inverted barometer effect or wind setup alone. Accordingly, this study aims to clarify the physical mechanisms responsible for the second surge peak observed during WCTS-type typhoons.
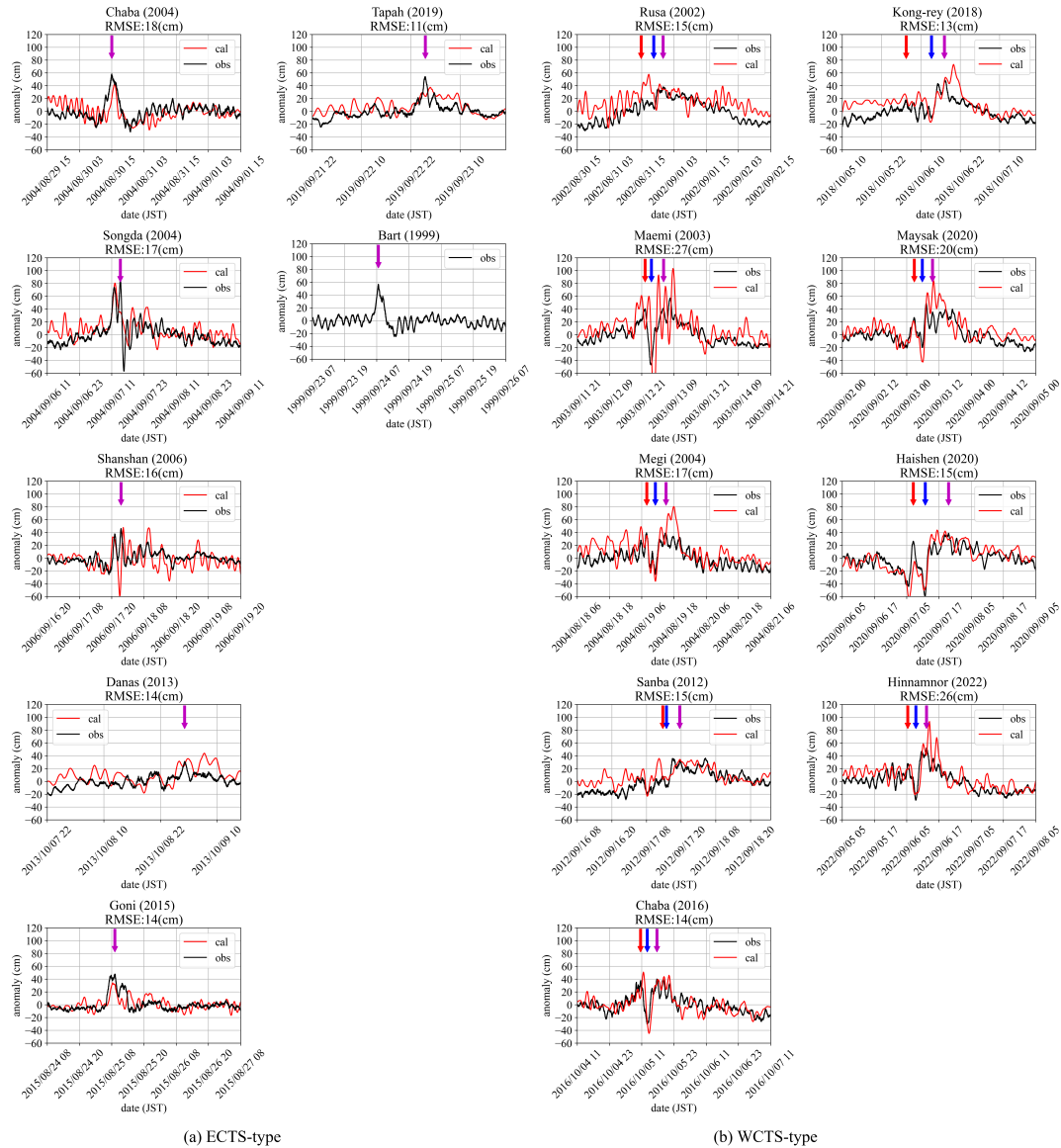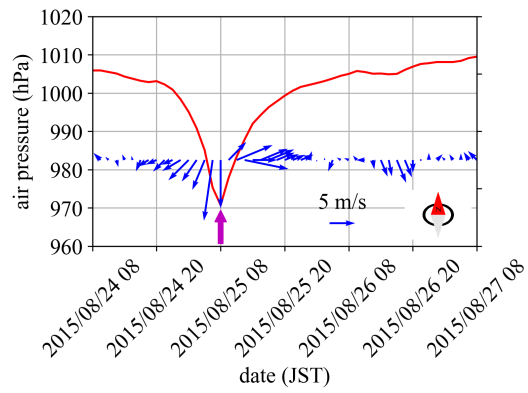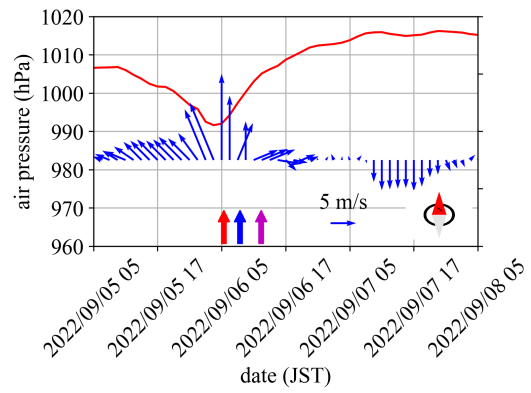

Figure 4. Time series of storm surge anomalies at the Hakata tidal station for (a) ECTS-type and (b) WCTS-type typhoons. The black curve represents the observed storm surge anomaly, while the red curve shows the simulated anomaly. Red, blue, and purple arrows indicate the timing of the first peak, local minimum, and second peak (or maximum), respectively.

(a) Goni (2015): ECTS-type   (b) Hinnamnor (2022): WCTS-type

Figure 5. Time series of air pressure and winds at Fukuoka weather station for (a) ECTS (Goni, 2015) and (b) WCTS (Hinnamnor, 2022) typhoons.

5 Numerical Simulation

5.1 Model Setup

An unstructured grid Finite-Volume Community Ocean Model (FVCOM, Chen et al. (2003)) was used to calculate storm surges associated with the input meteorological data for air pressure and wind. The FVCOM employs the finite-volume method, using a triangular grid system in the horizontal plane and generalized terrain-following coordinates in the vertical direction (Yoon and Shim (2013)). The model incorporates the modified level 2.5 (Mellor and Yamada (1982), Smagorinsky (1963)) turbulent closure schemes for vertical and horizontal mixing. Its governing equations include the following equations of motion and continuity equations:

$$\frac{\partial u}{\partial t} + u\frac{\partial u}{\partial x} + v\frac{\partial u}{\partial y} + w\frac{\partial u}{\partial z} - fv = -\frac{1}{\rho_0}\frac{\partial(p_H + p_a)}{\partial x} + \frac{\partial}{\partial z}\left(K_m\frac{\partial u}{\partial z}\right) + F_u, \tag{1}$$

$$\frac{\partial v}{\partial t} + u\frac{\partial v}{\partial x} + v\frac{\partial v}{\partial y} + w\frac{\partial v}{\partial z} + fu = -\frac{1}{\rho_0}\frac{\partial(p_H + p_a)}{\partial y} + \frac{\partial}{\partial z}\left(K_m\frac{\partial v}{\partial z}\right) + F_v, \tag{2}$$

$$\frac{\partial w}{\partial t} + u\frac{\partial w}{\partial x} + v\frac{\partial w}{\partial y} + w\frac{\partial w}{\partial z} = \frac{\partial}{\partial z}\left(K_m\frac{\partial w}{\partial z}\right) + F_w, \tag{3}$$

$$\frac{\partial u}{\partial x} + \frac{\partial v}{\partial y} + \frac{\partial w}{\partial z} = 0, \tag{4}$$

where x, y, and z are horizontal and vertical positions, u, v, and w are the velocities in the x, y, and z directions, respectively, t represents time, p_a is the air pressure on the sea surface, p_H is the hydrostatic pressure, f is the Coriolis parameter, g is the acceleration due to gravity, K_m is the vertical eddy viscosity, and F_u, F_v, and F_w are the horizontal and vertical momentum diffusion terms, respectively. The FVCOM utilizes the finite-volume method for discretization and can be applied using either Cartesian (xy) or geographic (latitude and longitude) coordinates. A detailed description of the discretization procedures is available in (Chen et al. (2003)).

The boundary conditions on the sea surface are defined as

$$K_m\left(\frac{\partial u}{\partial z}, \frac{\partial v}{\partial z}\right) = \frac{1}{\rho_0}(\tau_{sx}, \tau_{sy}), \tag{5}$$

$$w = \frac{\partial \eta}{\partial t} + u\frac{\partial \eta}{\partial x} + v\frac{\partial \eta}{\partial y} \tag{6}$$

where η is the height of the free surface, ρ_0 is the density of seawater, and τ_{sx} and τ_{sy} are the x- and y-axis components of the sea surface shear stress, respectively:

$$(\tau_{sx}, \tau_{sy}) = \rho_a C_s U(U_{10}, V_{10}), \tag{7}$$

$$U = \sqrt{U_{10}^2 + V_{10}^2} \tag{8}$$

with U_{10} and V_{10} being the x- and y-axis components of the wind speed 10 m above the sea surface, respectively, ρ_a being the density of the atmosphere, and C_s being the wind drag coefficient, which is calculated as follows (Large and Pond (1981)):

$$C_s = \begin{cases} 1.20 \times 10^{-3} & \text{if} \quad 0 \leq U < 11\text{m/s} \\ (0.49 + 0.065U) \times 10^{-3} & \text{if} \quad 11\text{m/s} \leq U \end{cases} \tag{9}$$

We adopted this formulation to be consistent with the wind stress setting used in Niimi et al. (2022), which provided a validated reference framework for storm surge simulations in this region.

The boundary conditions on the seafloor are defined as

$$K_m \left(\frac{\partial u}{\partial z}, \frac{\partial v}{\partial z} \right) = \frac{1}{\rho_0} (\tau_{bx}, \tau_{by}), \tag{10}$$

$$w = -u \frac{\partial h}{\partial x} - v \frac{\partial h}{\partial y} \tag{11}$$

where h is the water depth, and τ_{bx} and τ_{by} are the x- and y-axis components of the seafloor shear stress, respectively:

$$(\tau_{bx}, \tau_{by}) = \rho_0 C_b \sqrt{u^2 + v^2}(u, v). \tag{12}$$

The bottom drag coefficient is determined by matching a logarithmic bottom layer to the model at height z_a from the bottom:

$$C_b = \max \left(\kappa^2 / \ln \left(\frac{z_a}{z_0} \right)^2, 0.0025 \right) \tag{13}$$

where $k = 0.4$ is the von Kármán constant and z_0 is the bottom roughness parameter, which is 0.001 m in the ocean.

The model domain is depicted in Figure 6. This domain spans an extensive area from 125° to 135° E in longitude and from 27° to 36° N in latitude (Figure 6a). For the FVCOM input, we provided x–y coordinates corresponding to the longitude and latitude, respectively. Coastal lines were sourced from the Ministry of Land, Infrastructure, Transport, and Tourism of Japan (https://nlftp.mlit.go.jp/ksj/gml/datalist/KsjTmplt-C23.html). Water depth data were obtained from the Japan Hydrographic Association (https://www.jha.or.jp/jp/shop/products/btdd/) and Japan Oceanographic Data Center (https://www.jodc.go.jp/jodcweb/JDOSS/infoJEGG_j.html), and they were interpolated into the mesh using an inverse distance weighting method. A large unstructured grid with a resolution of 50 km was used for the open sea, whereas very small triangular meshes with a resolution of 300 m were employed along Kyushu Island and Hakata Bay. The model used three sigma levels in the vertical direction. The triangular grid comprised 254,335 nodes and 483,582 elements. Winds at a height of 10 m above the sea surface and air pressure at the sea surface were obtained from Meso-Scale Model (MSM, https://www.data.jma.go.jp/suishin/cgi-bin/catalogue/make_product_page.cgi?id=MesModel), which provided grid point values from an hourly weather forecast for Japan and its surrounding ocean area calculated at a finer grid spacing (5 km) than the global model. In addition, we conducted three simulation cases: (1) both atmospheric pressure and wind forcing, (2) pressure-only forcing, and (3) wind-only forcing. For each typhoon, the computation period was 8 days with a timestep of 1.0 s. The initial water level was set at mean sea level, and tides and wind waves were not considered. For typhoon Bart (1999), no calculated values are available due to the absence of MSM.
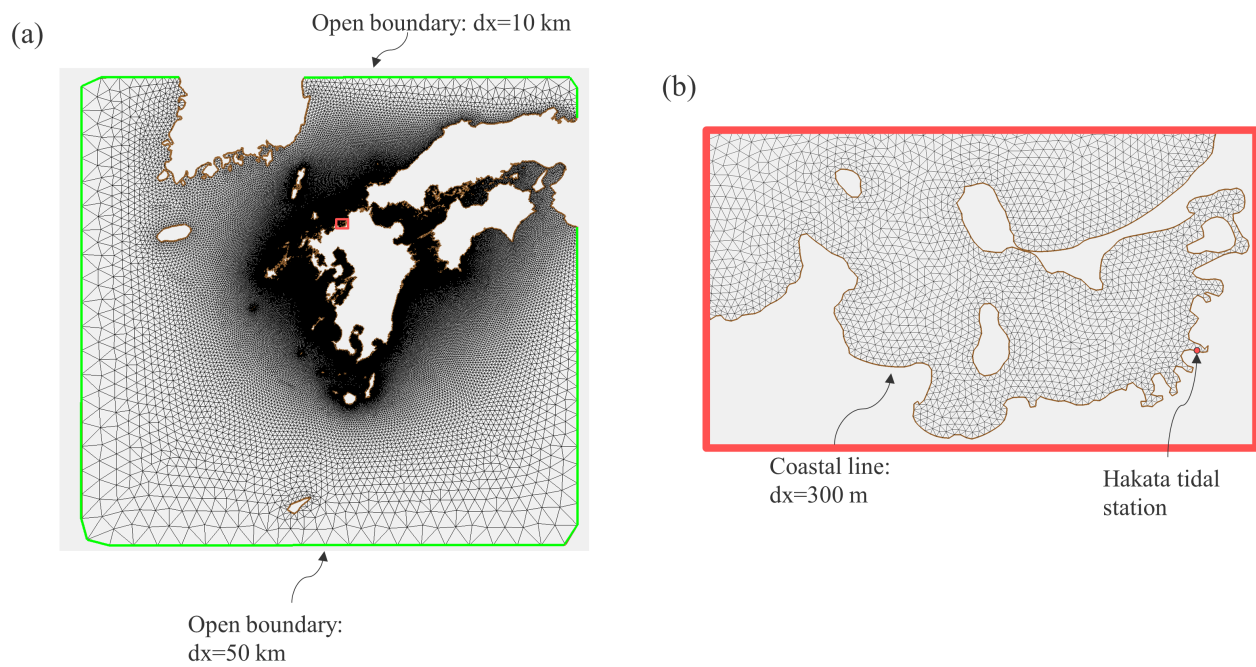
(a)

Open boundary: dx=10 km

(b)

Open boundary:
dx=50 km

Coastal line:
dx=300 m

Hakata tidal
station

Figure 6. Overview of model domain: (a) grid composition and (b) enlarged grid view of Hakata Bay.

5.2 Validation

Red lines in Figure 4 show the time series of storm surge anomalies at the Hakata tidal station for both WCTS and ECTS typhoons, as simulated by FVCOM. Below each panel title, the root mean square error (RMSE) between the observed and simulated surge anomalies is indicated as a quantitative measure of model accuracy. Overall, the general trend of the observed time series is well reproduced by the model. Particularly, the simulated results clearly capture the unusual temporal patterns of storm surge anomalies during WCTS-type typhoons and the 2-hour periodic seiche in Hakata Bay, as reported by Yamashiro et al. (2016).

5.3 Contributions of Pressure and Wind to Storm Surge Anomalies

Table 1 shows the correlation coefficient and RMSE between the storm surge anomalies simulated under combined wind and pressure forcing and the sum of the individually simulated wind-only and pressure-only cases in Hakata Bay. For all typhoons, the correlation coefficient was nearly 1, and the RMSE was extremely small.

These results indicate that the storm surge anomalies generated under simultaneous wind and pressure forcing can be decomposed into the sum of the individual surge components induced by wind and pressure, respectively—implying that the two effects act independently. In the following sections, we examine the development of storm surge anomalies under combined atmospheric pressure and wind forcing by decomposing the total surge into its pressure- and wind-driven components. We approximated the total storm surge anomaly as the linear sum of the pressure-induced and wind-induced components, as follows:

$$\eta_{\mathrm{pres+wind}} \approx \eta_{\mathrm{pres}} + \eta_{\mathrm{wind}} \tag{14}$$

where η_{pres} is the sea level anomaly caused by atmospheric pressure alone, η_{wind} is the sea level anomaly caused by wind forcing alone, and $\eta_{\mathrm{pres+wind}}$ is the sea level anomaly resulting from the combined effects of pressure and wind forcing We then investigate the specific factors contributing to the development of each component.

Table 1. Correlation coefficient (R) and root mean square error (RMSE) between the simulated storm surge anomalies in Hakata Bay under combined wind and pressure forcing ($\eta_{\mathrm{pres+wind}}$), and the sum of two separate simulations with pressure-only and wind-only forcing ($\eta_{\mathrm{pres}} + \eta_{\mathrm{wind}}$).

Typhoon type	Typhoon name (year)	R	RMSE (cm)
WCTS-type	Rusa (2002)	0.980	2.853
	Maemi (2003)	0.979	4.076
	Megi (2004)	0.986	2.399
	Sanba (2012)	0.963	2.913
	Chaba (2016)	0.963	3.317
	Kong-rey (2018)	0.971	2.912
	Maysak (2020)	0.981	3.296
	Haishen (2020)	0.979	3.087
	Hinnamnor (2022)	0.956	4.494
ECTS-type	Chaba (2004)	0.970	2.585
	Songda (2004)	0.981	2.593
	Shanshan (2006)	0.965	3.250
	Danas (2013)	0.988	1.757
	Goni (2015)	0.984	1.429
	Tapah (2019)	0.932	3.214

We investigated the cause and characteristics of the second peak shown in WCTS typhoons by conducting a detailed analysis of the spatial distribution of storm surge anomalies, wind, and atmospheric pressure during Hinnamnor (2022), a representative WCTS typhoon.

Figure 7 shows the spatial distribution of the storm surge anomaly during Hinnamnor (2022). Panel (a) shows $\eta_{\mathrm{pres+wind}}$, panel (b) depicts η_{pres}, and panel (c) presents η_{wind}. Figure 8 shows the spatial distribution of atmospheric pressure and wind. The top graphs of Figure 9 show the time series of η_{pres} and η_{wind} at the Hakata tidal station. At 02:00 on September 6, 2022, the typhoon enters the Tsushima Strait. At this time, the sea level rises according to the low air pressure distribution around the typhoon center (Figures 7b0 and 8a0), resulting in a sea level rise of approximately 20 cm in Hakata Bay at the center of the NCKI (top graph in Figure 9a). The storm surge anomalies induced by winds gradually increases from the NCKI toward the SCKP, forming a gradient (Figure 7c0). This is because the wind blows toward the SCKP, causing an increase in storm surge anomalies due to the wind setup (Figure 8b0). At 05:00 on September 6, 2022, the typhoon is near the SCKP and at the closest point to the NCKI. With only atmospheric pressure present, a positive anomaly develops around the typhoon, leading to a positive anomaly throughout the Tsushima Strait (Figure 7b1). The distribution of the positive anomalies corresponds to that of the low-pressure system (Figure 8a1). As a result, the storm surge anomalies in Hakata Bay increases by approximately 20 cm owing to the inverted barometer effect (top graph in Figure 9a). When wind is present, positive anomalies appear along the SCKP and NCKI, although their values are small (Figure 7c1). By 08:00 on September 6, 2022, as the typhoon enters the Sea of Japan, a negative anomaly develops in the Tsushima Strait (Figure 7a2), mainly derived from the wind-induced anomaly (Figure 7c2). By 11:00 on September 6, 2022, as the typhoon continues northeastward in the Sea of Japan, a positive anomaly appears in the NCKI (Figure 7a3), mainly derived from the positive wind-induced anomaly (Figure 7c3). By 14:00 on September 6, 2022, the positive anomaly in the NCKI intensifies, resulting in a second peak at NCKI (Figure 7a4), mainly derived from positive anomalies induced by both air pressure and wind (Figures 7b4 and 7c4). The atmospheric pressure across the Tsushima Strait reaches near-normal levels, and the wind speeds are below 10 m/s after 08:00 on September 6, 2022 (Figures 8a2–a4 and 8b2–b4). Consequently, the only forces acting on the seawater in the Tsushima Strait are gravity and the Coriolis force, with no external forces notably increasing the storm surge anomalies. The second peak appears from the superposition of oscillations generated in the Tsushima Strait by atmospheric pressure and wind, with the second peak occurring in the NCKI region when the peaks of these oscillations coincide.
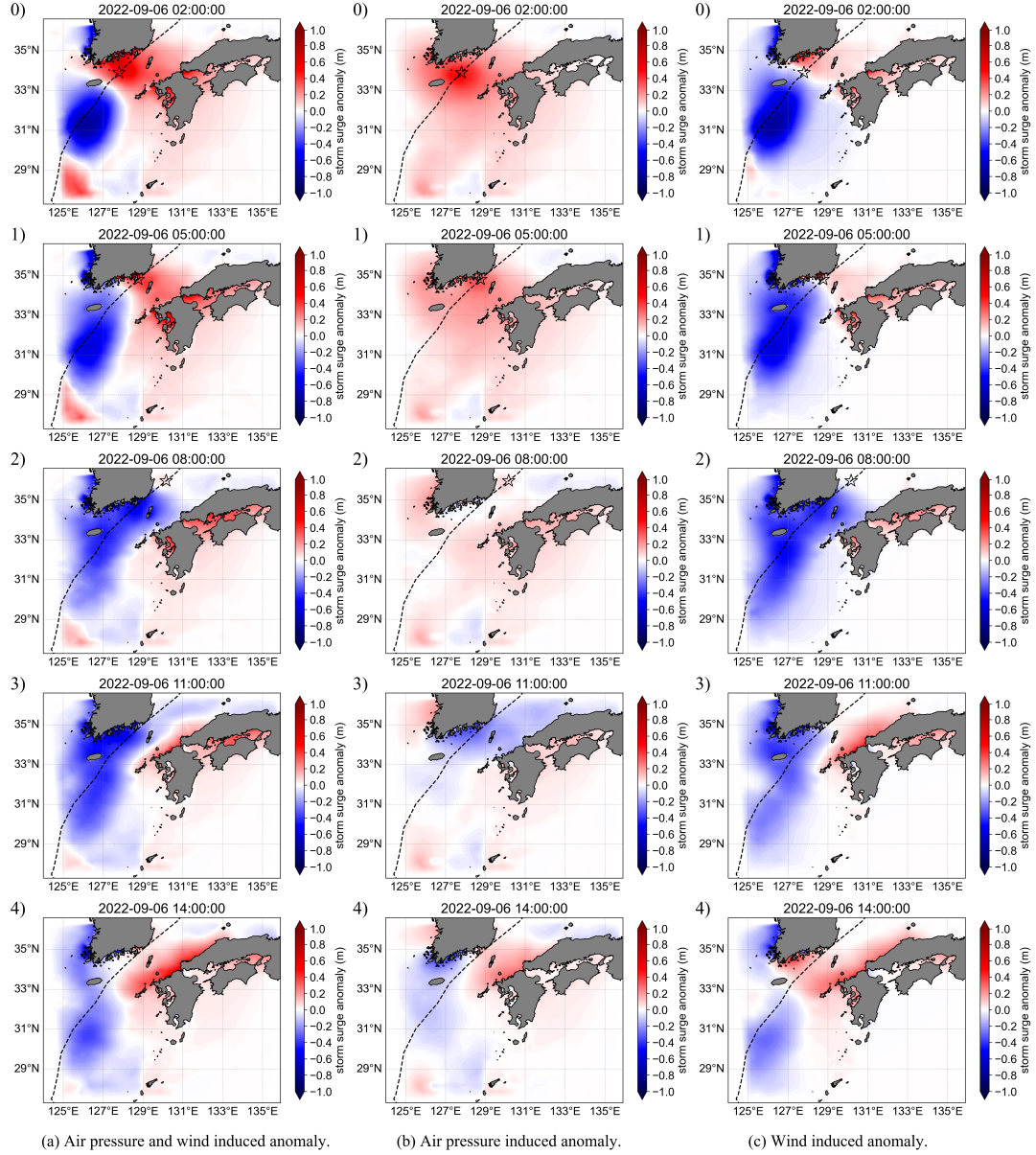
Figure 7. Distribution of storm surge anomalies during Typhoon Hinnamnor (2022). The black line represents the typhoon track, and the black star marks the typhoon center. (a) Storm surge anomaly resulting from the combined effects of atmospheric pressure and wind forcing ($\eta_{\mathrm{pres+wind}}$). (b) Storm surge anomaly driven by atmospheric pressure alone (η_{pres}). (c) Storm surge anomaly driven by wind forcing alone (η_{wind}).
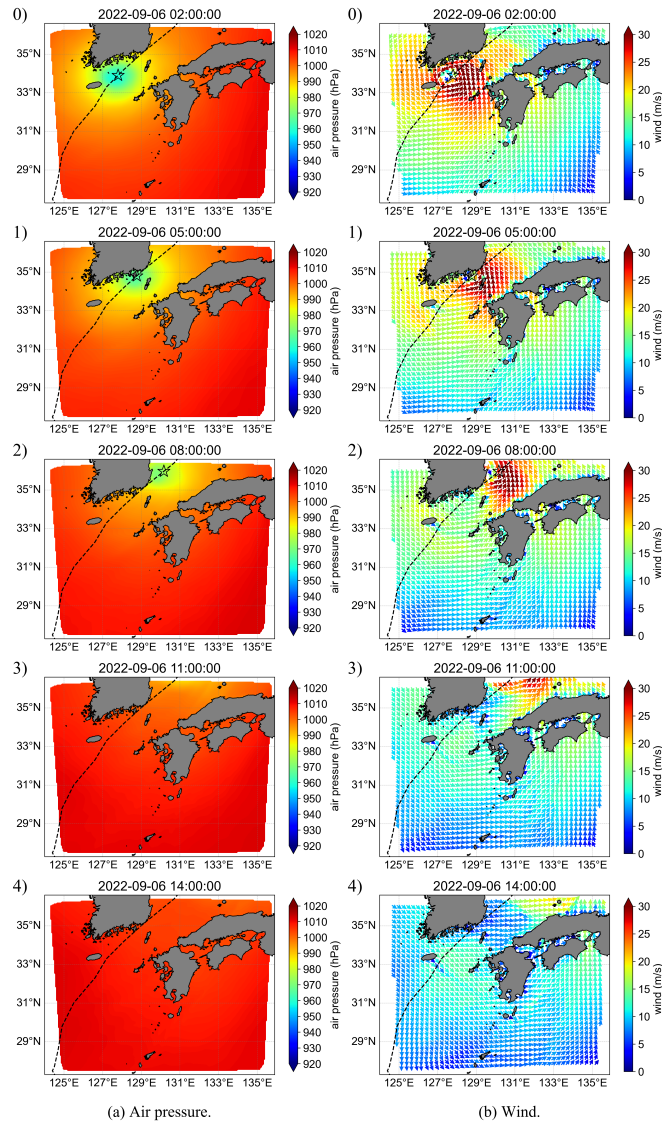
(a) Air pressure. (b) Wind.

Figure 8. Distributions of (a) air pressure and (b) wind during typhoon Hinnamnor (2022). The black curve indicates the typhoon path, and the black star indicates the typhoon center.

6 Spectral Analysis using Wavelet Transform

6.1 Continuous Wavelet Transform

We performed a spectral analysis using the continuous wavelet transform (CWT) to investigate oscillatory components within storm surge anomalies. The CWT is well-suited for analyzing nonstationary signals, as it enables time–frequency localization of transient features. It uses a base function, known as the mother wavelet, which is scaled and shifted to compare with the signal of interest, allowing for frequency decomposition over time. The mother wavelet is given by

$$\psi_{a,b}(t) = \frac{1}{\sqrt{a}}\psi\left(\frac{t-b}{a}\right) \tag{15}$$

where $\psi(t)$ is the mother wavelet, t denotes time, a is the scale, and b is the shift. When a increases, the mother wavelet stretches, making it more suitable for analyzing long waves. An increase in b results in a parallel shift in the positive direction along the time axis. For the mother wavelet defined by scale a and shift b, denoted by $\psi_{a,b}(t)$, the CWT is defined as

$$W_{\psi_{a,b}}[x(t)] = \int_{-\infty}^{\infty} x(t)\psi_{a,b}^{*}(t)dt \tag{16}$$

where $x(t)$ is the signal of interest and $*$ denotes the complex conjugate. By continuously varying scale a and shift b, the CWT is a mapping onto a two-dimensional plane of (a,b), allowing frequency analysis in the time domain. We use the following complex Morlet wavelet as the mother wavelet:

$$\psi(t) = \frac{1}{\sqrt{\pi B}}\exp\left(-\frac{t^2}{B}\right)\exp(2\pi Cjt) \tag{17}$$

where j is the imaginary unit, $B = 1.5$ is the bandwidth, and $C = 1.0$ is the center frequency. These values are recommended and lead to a high resolution and reduced artifacts (Lee et al. (2019)).

6.2 Dominant Oscillation Modes Identified by CWT

We analyze the factors that contribute to the second peak during the passage of a WCTS typhoon. As shown in Figure 4 and 7, the storm surge anomaly fluctuates because of the superposition of oscillations. To identify the oscillatory components other than tidal constituents in the time series of storm surge anomalies in Hakata Bay, the CWT was applied. The lower graphs in Figure 9 present the CWT scalograms, where atmospheric pressure (panel a) and wind (panel b) are independently imposed as external forces. Figure 10 shows the time series of these oscillatory components—2, 5, and 10 hours—extracted using the inverse CWT.

In both cases, three dominant oscillations with periods of 10, 5, and 2 hours are observed from 05:00 on September 6, 2022 to 17:00 on September 7, 2022. The 2-hour oscillation component has a maximum amplitude of approximately 10 cm, regardless of whether the external forcing is atmospheric pressure or wind, and the times of maximum amplitude coincided

((Figure 10a)). On the other hand, for the 5- and 10-hour oscillations, the maximum amplitude for the 5-hour oscillation ranges from 10 to 15 cm, with wind forcing resulting in an amplitude approximately 1.5 times larger than that caused by atmospheric pressure. The phase of the 5-hour oscillation is also about 2 hours earlier under wind forcing (Figure 10b).

290 Similarly, for the 10-hour oscillation, the peak occurs approximately 2 hours earlier when the wind is the external force (Figure 10c). The maximum amplitude is observed between 11:00 and 17:00 on September 6, 2022, which corresponds to the second peak of the storm surge anomaly, after which the amplitude gradually decreases. Compared to the 5-hour oscillation, the 10-hour oscillation component persists for a longer duration.

 Figures 11 and 12 show the spatial distributions of the 5 and 10-hour period oscillatory components in the Tsushima Strait.
295 For the 5-hour period oscillation, regardless of the external force, the Tsushima Island, the boundary between the East China Sea and Tsushima Strait and that between the Sea of Japan and Tsushima Strait act as nodes, while the SCKP and NCKI serve as antinodes. In addition, the SCKP and NCKI cells are in opposite phases. The timing of the oscillation depends on the external force. When atmospheric pressure is the external force (Figure 11a), the oscillation begins at 07:00 on September 6, 2022, when the typhoon is located on the eastern coast of Korea. When wind is the external force (Figure 11b), the oscillation
300 starts at 05:00 on September 6, 2022, when the typhoon is located near the SCKP, with the wind force occurring 2 hours earlier.

 For the 10-hour period oscillation, the boundary between the East China Sea and Tsushima Strait and that between the Sea of Japan act as nodes, while the Tsushima Island, SCKP, and NCKI serve as antinodes. Unlike the 5-hour period oscillation, the SCKP and NCKI are in the same phase. The timing of the 10-hour period oscillation is similar to that of the 5 h period oscillation, with wind force occurring 2 hours earlier.
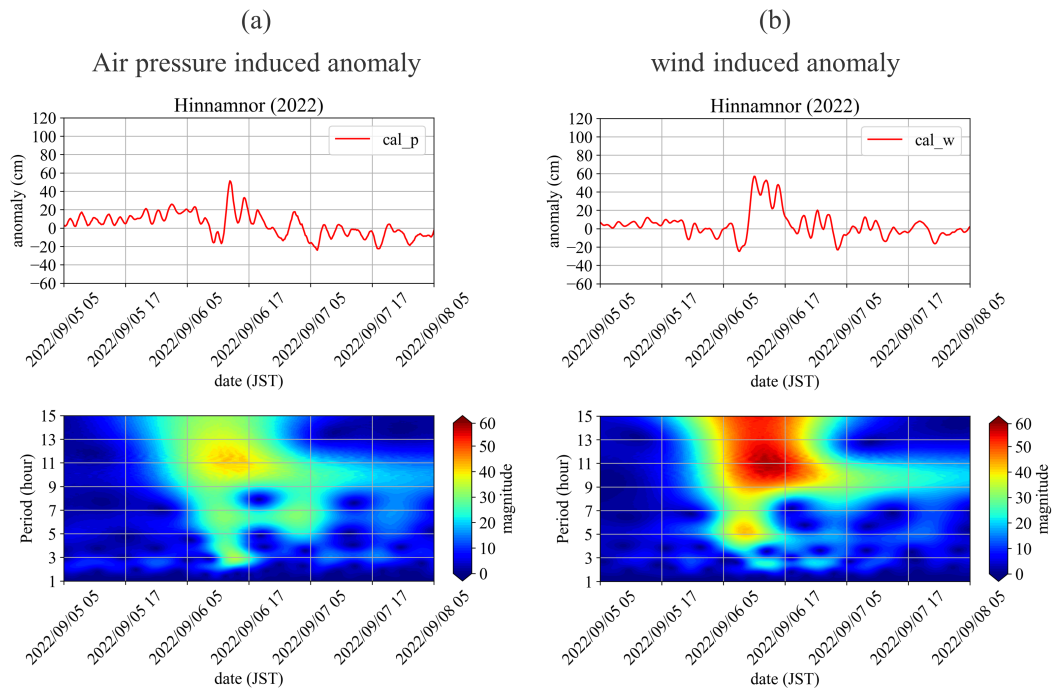
Figure 9. Simulated time series and scalograms at Hakata tidal station for anomalies induced by (a) air pressure and (b) wind.
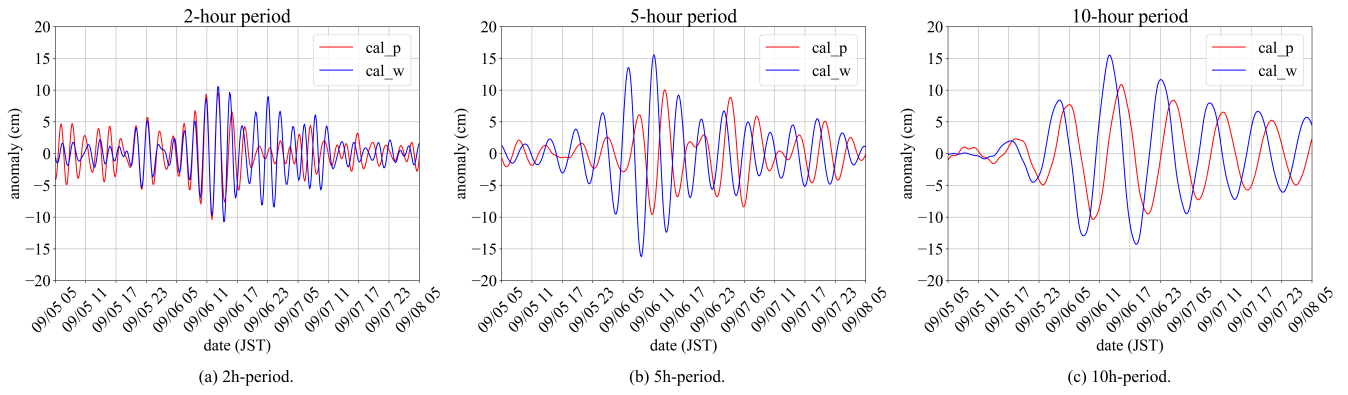
Figure 10. Time series of oscillatory components with periods of (a) 2 h, (b) 5 h, and (c) 10 h at Hakata tidal station obtained by inverse CWT. The red and blue curves indicate the anomalies induced by air pressure and wind, respectively.
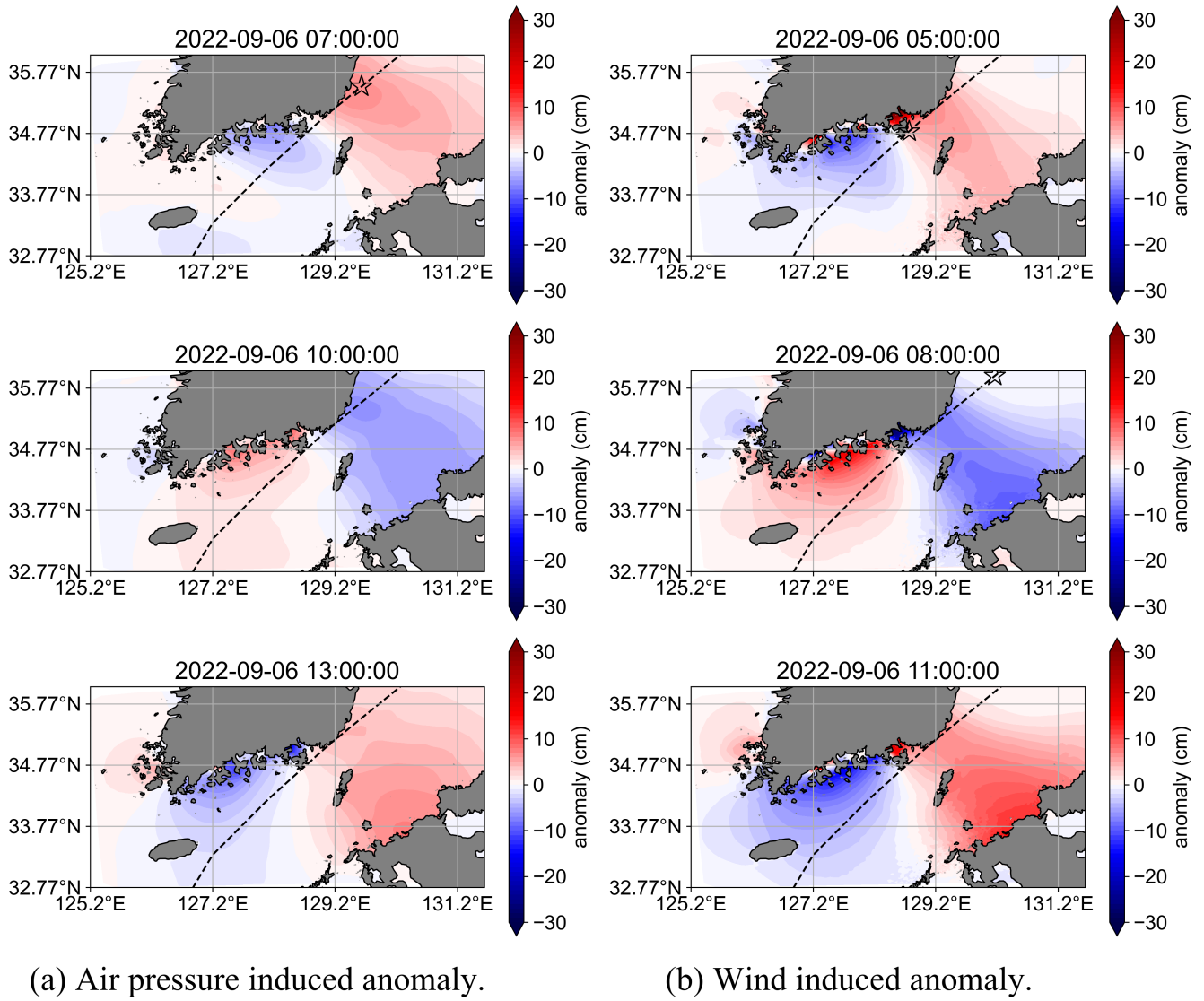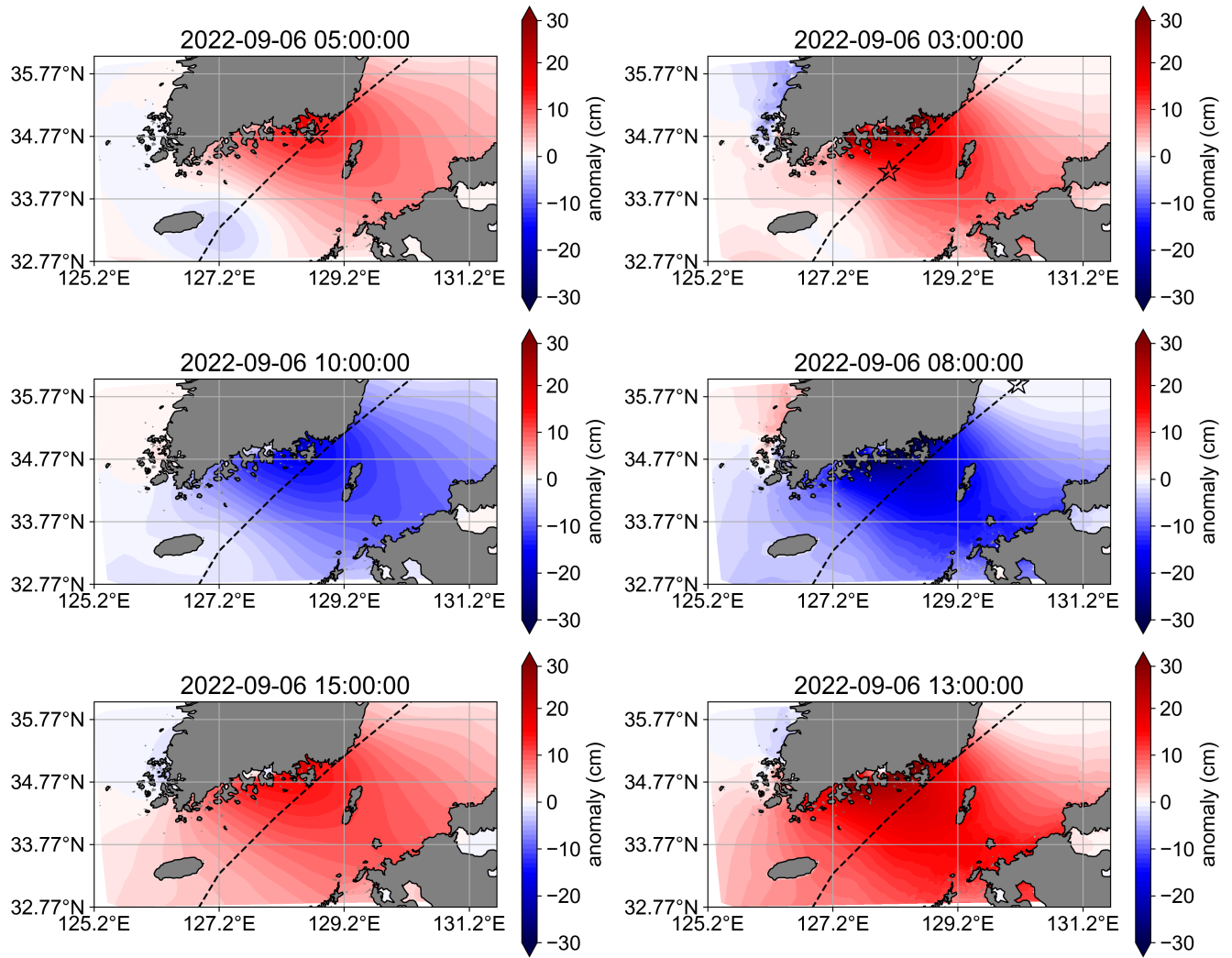
22

(a) Air pressure induced anomaly.

(b) Wind induced anomaly.

Figure 11. Distribution of 5 h period oscillations in Tsushima Strait for anomalies induced by (a) air pressure and (b) wind.

(a) Air pressure induced anomaly.　　　(b) Wind induced anomaly.

Figure 12. Distribution of 10 h period oscillations in Tsushima Strait for anomalies induced by (a) air pressure and (b) wind.

7 Discussion

The timing of oscillation generation differs between external forces as shown in Figures 11 and 12. This is owing to variations in the constraint-removal timing. In the pressure-only case, the storm surge anomalies along the SCKP reached its maximum at 05:00 on September 6, 2022, when the typhoon was closest to the SCKP (Figures 7b1 and 8a1). After this point, as the typhoon moved into the Sea of Japan, the external forcing diminished, and oscillations with 10-hour and 5-hour periods began to develop. In contrast, in the wind-only case, the maximum storm surge anomaly along the SCKP occurred earlier, at 02:00 on September 6, 2022 (Figures 7c0 and 8b0), a few hours before the typhoon reached its closest approach. This is because, at that time, the wind was directed toward the SCKP, generating a strong wind setup and resulting in a significant storm surge at the SCKP. As the typhoon reached its closest to the SCKP at 05:00, the wind direction shifted substantially, releasing the constraint on the water and initiating oscillatory motion. Therefore, in the wind-only case, the external forcing was released earlier than in the pressure-only case, leading to an earlier onset of oscillations. As the total storm surge anomaly is represented as the linear sum of the pressure-induced and wind-induced components, the NCKI experiences a higher and more prolonged storm surge compared to the cases with only one forcing component (Figures 7a3 and a4).

As shown in Figure 1b, there is a large change in water depth at the boundary between the Tsushima Strait and Sea of Japan. When such discontinuous change in the water depth occurs, the amplitude of the oscillations decreases exponentially near the discontinuity. For example, the waveform of the edge waves when the water depth changes discontinuously is described as follows:

$$\eta_1 = a\cos(\mu_1 x)\cos(ky + \sigma t) \tag{18}$$

$$\eta_2 = a\cos(\mu_1 l)e^{-\mu_2(x-l)}\cos(ky + \sigma t) \tag{19}$$

$$\mu_1 = \sqrt{\frac{\sigma^2}{gh_1} - k^2}, \quad \mu_2 = \sqrt{k^2 - \frac{\sigma^2}{gh_2}} \tag{20}$$

Let the coastline lie along the y axis, with $x > 0$ representing the sea. The water depth and width of the continental shelf are denoted as h_1 and l, respectively. The water depth of the deep sea is h_2, where $h_1 < h_2$ (i.e., the depth of deep sea is greater than that of the continental shelf). The wave number and angular frequency are represented by k and σ, respectively, where $a > 0$ is a constant. According to Equation (19), the oscillation amplitude in the region where $x > l$ (i.e., deeper area) becomes substantially smaller than that in the region where $x < l$ because of the discontinuous change in the water depth.

This phenomenon arises because of the properties of long waves. The group velocity of long waves is expressed as $C = \sqrt{gh}$, indicating that waves move more slowly in shallow regions and faster in deeper regions. Consequently, when long waves generated in shallow regions propagate toward deeper areas, their group velocity increases rapidly due to the depth transition. This abrupt change in wave speed hinders the efficient transmission of wave energy into deeper waters, resulting in partial reflection of the incoming waves—similar to encountering a fixed boundary at the depth discontinuity. The interaction between the reflected and incoming waves gives rise to standing waves, establishing a fluid oscillatory system dominated by specific natural oscillation periods.

Consequently, oscillations do not occur in much deeper regions, leading to node formation. Hence, the 5 and 10 h period oscillations are confined to the shallow regions where these standing wave patterns develop.

Here, we examine the reasons behind the 5 h period oscillation creating a node in the region between the SCKP and NCKI near the Tsushima Island. This phenomenon is related to oscillation without the Coriolis force. By solving the wave equation, we obtain

$$\frac{\partial^2 \eta}{\partial t^2} = c^2 \left(\frac{\partial^2 \eta}{\partial x^2} + \frac{\partial^2 \eta}{\partial y^2} \right) \tag{21}$$

$$c = \sqrt{gh} \tag{22}$$

in a rectangular domain with dimensions $b \times l$, where depth h is constant and ensures that the solution satisfies the following boundary conditions:

$$v = 0, \quad (y = 0, b) \tag{23}$$

$$\eta = 0, \quad (x = 0, l) \tag{24}$$

The following solution is obtained:

$$\eta = A \sin(kx) \cos(k'y) \sin(\sigma t) \tag{25}$$

$$k = \frac{m}{l}\pi, \quad k' = \frac{n}{b}\pi, \quad \sigma = c\sqrt{k^2 + k'^2} \tag{26}$$

where m and n are integers representing the vibration modes in the x- and y-axis directions, respectively. Additionally, the oscillation period is given by

$$T_{m,n} = \frac{2\pi}{\sigma} = \frac{2}{\sqrt{gh}} \left\{ \left(\frac{m}{l}\right)^2 + \left(\frac{n}{b}\right)^2 \right\}^{-1/2} \tag{27}$$

For the spatial scale of the Tsushima Strait, with $h = 80$ m, $l = 550$ km, $b = 250$ km, and $A = 5$ cm, the solutions for $(m,n) = (1,1), (1,0)$ are presented in Equation (25) and depicted in Figure 13. The oscillation with $(m,n) = (1,1)$ has nodes at $x = 0$ and l, $y = \frac{b}{2}$, and antinodes at $x = \frac{l}{2}$, $y = 0$ and b. The oscillation with $(m,n) = (1,1)$ has nodes at $x = 0$ and l and $y = \frac{b}{2}$ and antinodes at $x = \frac{l}{2}$ and $y = 0$ and b. The period of this oscillation is $T_{1,1} = 4.52$ h. In addition, the oscillation with $(m,n) = (1,0)$ has nodes at $x = 0$ and l and antinodes at $x = \frac{l}{2}$. The period of this oscillation is $T_{1,0} = 10.91$ h. These periods correspond to the 5 and 10 h periods observed in the CWT and show that these oscillations cause delayed storm surges. The sea level differences observed at Izuhara (located on Tsushima Island) and Busan (in SCKP) during typhoon passages through the strait, as reported by Yi (1970), are likely associated with the 10 and 5-hour period oscillation modes.

The above discussion was conducted under the assumption of no Coriolis force; however, Wu et al. (2021) demonstrated that the tidal dynamics (K2 and M2) in the Tsushima Strait are primarily governed by Kelvin waves and partial reflection of Kelvin waves occurs at the junction between the Tsushima Strait and the Japan Sea. The identified oscillations propagated with the coastline on their right, which is consistent with the typical propagation direction of Kelvin waves in the Northern Hemisphere. This suggests that the observed oscillatory behavior is strongly influenced by the characteristics of Kelvin waves.

Niimi et al. (2022) compared numerical simulations of Typhoon Maysak (2020) with and without the Coriolis force and found that the second storm surge peak at the NCKI was significantly reduced when the Coriolis force was excluded. Notably, the 10-hour oscillation component still appeared even in the absence of the Coriolis force; however, the 5-hour oscillation component vanished. This indicates that the 5-hour oscillation identified through continuous wavelet transform (CWT) analysis is highly sensitive to and likely governed by the Coriolis force.

Furthermore, among WCTC-type typhoons, those that travel northward through the Tsushima Strait—such as Maysak (2020) and Haishen (2020)—tend to produce a second storm surge peak that is both larger and longer-lasting. This is likely due to the continued southwesterly winds following the typhoon's passage, which induced Ekman transport. Even minor variations in typhoon tracks can lead to differences in the persistence of storm surge anomalies. In future research, we aim to identify WCTS-type typhoons that generate the most hazardous storm surges by considering the combined effects of Ekman transport, oscillations in the (1,1) and (1,0) modes, and the timing of the release of external forcing.

Given the potential for the delayed storm surges caused by WCTS-type typhoons, even after an first peak in water levels, it's crucial that we don't prematurely assume safety. Therefore, we believe it's essential to implement measures that extend the period during which people remain evacuated, preventing them from returning home too soon. Moreover, future climate change, characterized by increased typhoon intensity and sea-level rise, could lead to unforeseen inundation in areas previously unaffected. Therefore, to prepare for such flooding, it's crucial for the relevant coastal regions to take measures. These include elucidating the mechanisms of water level rise and establishing predictive methods for these phenomena.
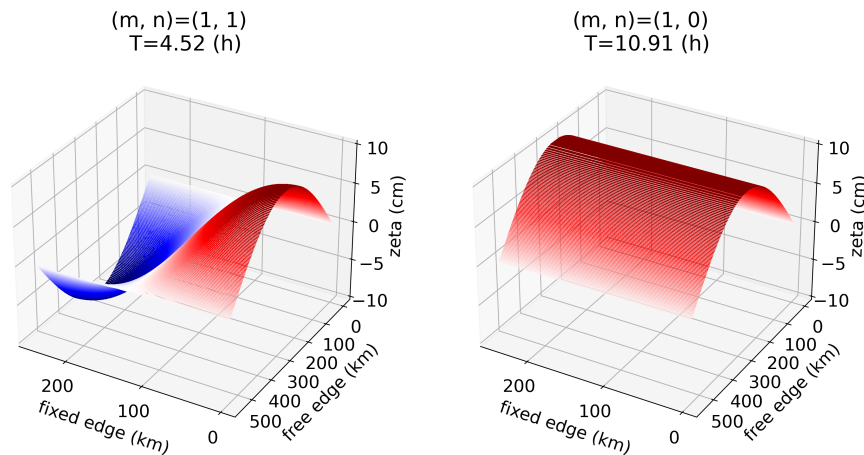

Figure 13. Solutions of wave equation, where m and n represent the mode of vibration in the free- and fixed-edge directions, respectively. The color code indicates the zeta value.

8 Conclusions

385 In this study, we investigated the mechanisms behind storm surge development along the NCKI using observational data, storm surge numerical simulations, and CWT. Typhoons that induce large storm surges in the NCKI can be categorized based on their tracks—either approaching from the ECTS or from the SCKP through the WCTS.

For ECTS-type typhoons, storm surge peaks occur when the typhoon is closest to the NCKI. At this point, atmospheric pressure reaches its minimum, and northerly winds drive seawater toward the coast, resulting in a surge. This behavior is well

390 explained by the inverted barometer effect and wind setup. In contrast, WCTS-type typhoons display a more complex pattern. The storm surge initially peaks as the typhoon nears the NCKI, then rapidly declines, followed by a second, larger peak after the typhoon has passed. At the time of this second peak, atmospheric pressure has returned to near-normal levels and wind speeds are low, rendering typical storm surge mechanisms—such as the barometer effect and wind setup—inadequate to explain the surge.

395 Spectral analysis using the CWT revealed a continuous 2-hour periodic oscillation localized in Hakata Bay, along with the emergence of 5- and 10-hour oscillations following the initial surge peak. To investigate the spatial characteristics of these longer-period oscillations, we conducted storm surge simulations and applied CWT analysis to the resulting spatial data. The 5-hour oscillation, with antinodes at the NCKI and SCKP and a node at Tsushima Island located in the center of the strait, corresponds to the (1,1) natural oscillation mode of the Tsushima Strait. The 10-hour oscillation represents the (1,0) mode.

400 These oscillations are triggered by the release of potential energy stored within the strait after the typhoon exits into the Sea of Japan. The 5-hour mode appears to be strongly influenced by the Coriolis force, as suggested by prior numerical experiments. The superposition of these (1,0) and (1,1) modes leads to the delayed second peak observed in NCKI storm surges.

We identified an anomalous storm surge phenomenon associated with typhoons passing through semi-enclosed straits under specific conditions and conducted a detailed investigation of the underlying mechanisms. Our findings emphasize the critical

405 role of resonance effects in such straits, offering new insights into storm surge risks under particular typhoon scenarios. These mechanisms are not unique to the Tsushima Strait and may occur in other regions where typhoons or low-pressure systems pass through similar strait geometries. Importantly, variations in oscillation period, amplitude, and modal structure can lead to differences in the timing and magnitude of storm surges across different locations. Future climate change, with increased typhoon intensity and sea-level rise, may cause unexpected flooding in previously unaffected areas. Therefore, it's crucial for

410 coastal regions to prepare by understanding the mechanisms of water level rise and developing predictive methods.

Author contributions. Conceptualization, Shinichiro Ozaki, Yoshihiko Ide and Masaru Yamashiro; Data curation, Shinichiro Ozaki; Formal analysis, Shinichiro Ozaki; Funding acquisition, Shinichiro Ozaki; Investigation, Shinichiro Ozaki and Yoshihiko Ide; Methodology,

Declaration of generative AI and AI-assisted technologies in the writing process

During the preparation of this work, the authors used ChatGPT to improve language. After using this tool, the authors reviewed and edited the content as needed. The authors take full responsibility for the content of the publication.

References

425

Balaguru, K., Judi, D., and Leung, L.: Future hurricane storm surge risk for the U.S. gulf and Florida coasts based on projections of thermo-
dynamic potential intensity, Climatic Change, 138, 99–110, https://doi.org/10.1007/s10584-016-1728-8, 2016.

Bhaskaran, P. K., Rao, A. D., and Murty, T.: Tropical Cyclone–Induced Storm Surges and Wind Waves in the Bay of Bengal, pp. 237–294,
https://doi.org/https://doi.org/10.1002/9781119359203.ch17, 2020.

430 Bilskie, M. V., Hagen, S. C., Medeiros, S. C., Cox, A. T., Salisbury, M., and Coggin, D.: Data and numerical analysis of astronomic tides,
wind-waves, and hurricane storm surge along the northern Gulf of Mexico, Journal of Geophysical Research: Oceans, 121, 3625–3658,
https://doi.org/https://doi.org/10.1002/2015JC011400, 2016.

Chen, C., Liu, H., and Beardsley, R. C.: An Unstructured Grid, Finite-Volume, Three-Dimensional, Primitive Equations Ocean Model:
Application to Coastal Ocean and Estuaries, Journal of Atmospheric and Oceanic Technology, 20, 159 – 186, https://doi.org/10.1175/1520-
435 0426(2003)020<0159:AUGFVT>2.0.CO;2, 2003.

Hong, C.-H. and Yoon, J.-H.: The Effect of Typhoon on the Coastal Sea Level Variations in the Tsushima Straits, Oceanography in Japan, 1,
225–249, https://doi.org/10.5928/kaiyou.1.225, 1992.

Ide, Y., Kora, T., Kodama, M., Yamashiro, M., and Hashimoto, N.: LONG-TERM PROJECTION OF STORM SURGE CHARACTERIS-
TICS IN SUO-NADA SEA USING LARGE ENSEMBLE CLIMATE PROJECTION DATA, Journal of Japan Society of Civil Engineers,
440 Ser. B3 (Ocean Engineering), 76, I_1091–I_1096, https://doi.org/10.2208/jscejoe.76.2_I_1091, (in Japanese)., 2020.

Igarashi, Y. and and, Y. T.: Application of recurrent neural network for prediction of the time-varying storm surge, Coastal Engineering
Journal, 63, 68–82, https://doi.org/10.1080/21664250.2020.1868736, 2021.

Kennedy, A. B., Gravois, U., Zachry, B. C., Westerink, J. J., Hope, M. E., Dietrich, J. C., Powell, M. D., Cox, A. T., Luettich Jr, R. A., and
Dean, R. G.: Origin of the Hurricane Ike forerunner surge, Geophysical Research Letters, 38, 2011.

445 Kim, S., Matsumi, Y., Yasuda, T., and Mase, H.: Mechanism of Abnormal Storm Surges after Passage of Typhoons around
West Coasts of the Sea of Japan, Journal of Japan Society of Civil Engineers, Ser. B2 (Coastal Engineering), 66, 221–225,
https://doi.org/10.2208/kaigan.66.221, (in Japanese)., 2010.

Large, W. G. and Pond, S.: Open Ocean Momentum Flux Measurements in Moderate to Strong Winds, Journal of Physical Oceanography,
11, 324 – 336, https://doi.org/10.1175/1520-0485(1981)011<0324:OOMFMI>2.0.CO;2, 1981.

450 Lee, G. R., Gommers, R., Waselewski, F., Wohlfahrt, K., and O'Leary, A.: PyWavelets: A Python package for wavelet analysis, Journal of
Open Source Software, 4, 1237, https://doi.org/10.21105/joss.01237, 2019.

Mellor, G. L. and Yamada, T.: Development of a turbulence closure model for geophysical fluid problems, Reviews of Geophysics, 20,
851–875, 1982.

Miguel Esteban, Takahito Mikami, T. S. H. T. S. N. J. M. v. L.: CLIMATE CHANGE ADAPTATION IN TOKYO BAY: THE CASE FOR
455 A STORM SURGE BARRIER, Coastal Engineering Proceedings, 1, management.35, https://doi.org/10.9753/icce.v34.management.35,
2014.

Mori, S., Shimura, T., Miyashita, T., Webb, A., and Mori, N.: Future changes in extreme storm surge based on a maximum potential storm
surge model for East Asia, Coastal Engineering Journal, 64, 630–647, https://doi.org/10.1080/21664250.2022.2145682, 2022.

Nakajo, S., Fijiki, H., Kim, S., Mori, N., Shibutani, Y., and Yasuda, T.: AN PARAMETRIC STUDY ON POTENTIAL OF
460 STORM SURGE IN TOKYO BAY, Journal of Japan Society of Civil Engineers, Ser. B2 (Coastal Engineering), 71, I_199–I_204,
https://doi.org/10.2208/kaigan.71.I_199, (in Japanese)., 2015.

Niimi, M., Ide, Y., Yamashiro, M., Hashimoto, N., and Kodama, M.: A CASE STUDY OF STORM SURGE INUNDATION IN DOKAI BAY BY TYPHOON MAYSAK IN 2020 AND ITS GENERATION MECHANISM, Journal of Japan Society of Civil Engineers, Ser. B2 (Coastal Engineering), 78, I_217–I_222, https://doi.org/10.2208/kaigan.78.2_I_217, (in Japanese)., 2022.

465 Shen, J. and Gong, W.: Influence of model domain size, wind directions and Ekman transport on storm surge development inside the Chesapeake Bay: A case study of extratropical cyclone Ernesto, 2006, Journal of Marine Systems, 75, 198–215, 2009.

Smagorinsky, J.: General circulation experiments with the primitive equations: I. The basic experiment, Monthly weather review, 91, 99–164, 1963.

Soontiens, N., Allen, S. E., Latornell, D., Souëf, K. L., Machuca, I., Paquin, J.-P., Lu, Y., Thompson, K., and Korabel, V.: Storm Surges in

470 the Strait of Georgia Simulated with a Regional Model, Atmosphere-Ocean, 54, 1–21, https://doi.org/10.1080/07055900.2015.1108899, 2016.

Tkalich, P., Vethamony, P., Babu, M. T., and Malanotte-Rizzoli, P.: Storm surges in the Singapore Strait due to winds in the South China Sea, Natural Hazards, 66, 1345–1362, https://doi.org/10.1007/s11069-012-0211-8, 2013.

Walton, T. and Dean, R.: Influence of discrete step size on wind setup component of storm surge, Coastal Engineering, 56, 1005–1008,

475 https://doi.org/10.1016/J.COASTALENG.2009.05.003, 2009.

Wu, D., Fang, G., Wei, Z., and Cui, X.: Study of the tidal dynamics of the Korea Strait using the extended Taylor method, Ocean Science, 17, 579–591, https://doi.org/10.5194/os-17-579-2021, 2021.

Wu, G., Shi, F., Kirby, J. T., Liang, B., and Shi, J.: Modeling wave effects on storm surge and coastal inundation, Coastal Engineering, 140, 371–382, 2018.

480 Wunsch, C. and Stammer, D.: Atmospheric loading and the oceanic "inverted barometer" effect, Reviews of Geophysics, 35, 79–107, 1997.

Yamashiro, M., Sonoda, A., Yurino, A., Kubo, T., Yokota, M., and Hashimoto, N.: STUDY ON BASIC CHARACTERISTICS OF STORM SURGE IN HAKATA BAY, Journal of Japan Society of Civil Engineers, Ser. B3 (Ocean Engineering), 72, I_348–I_353, https://doi.org/10.2208/jscejoe.72.I_348, (in Japanese)., 2016.

Yang, J.-A., Kim, S., Son, S., Mori, N., and Mase, H.: Assessment of uncertainties in projecting future changes to extreme storm surge height

485 depending on future SST and greenhouse gas concentration scenarios, Climatic Change, pp. 1–18, https://doi.org/10.1007/s10584-020-02782-7, 2020.

Yi, S.-U.: Variations of Oceanic Condition and Mean Sea Level in the Korea Strait, pp. 125–142, https://doi.org/doi:10.1515/9780824885830-015, 1970.

Yoon, J. J. and Shim, J. S.: Estimation of storm surge inundation and hazard mapping for the southern coast of Korea, in: Journal of Coastal

490 Research, pp. 856–861, Coastal Education Research Foundation Inc., ISSN 15515036, https://doi.org/10.2112/si65-145.1, 2013.

Yoon, J. J., Shim, J. S., Park, K. S., and Lee, J. C.: Numerical experiments of storm winds, surges, and waves on the southern coast of Korea during Typhoon Sanba: the role of revising wind force, Natural Hazards and Earth System Sciences, 14, 3279–3295, https://doi.org/10.5194/nhess-14-3279-2014, 2014.

Zhang, W.-Z., Shi, F., Hong, H.-S., Shang, S.-P., and Kirby, J. T.: Tide-surge Interaction Intensified by the Taiwan Strait, Journal of Geo-

495 physical Research: Oceans, 115, https://doi.org/https://doi.org/10.1029/2009JC005762, 2010.